Earth Planets Space, **59**, 1219–1229, 2007

Consistency between the flow at the top of the core and the frozen-flux approximation

K. A. Whaler[1] and R. Holme[2]

[1]*School of GeoSciences, University of Edinburgh, West Mains Road, Edinburgh, EH9 3JW, Scotland*
[2]*Department of Earth and Ocean Sciences, University of Liverpool, 4 Brownlow St., Liverpool, L69 3GP, England*

(Received March 13, 2007; Revised October 26, 2007; Accepted October 30, 2007; Online published January 11, 2008)

The flow just below the core-mantle boundary is constrained by the radial component of the induction equation. In the Alfvén frozen-flux limit, thought to be applicable to the outer core on the decade timescale of interest in geomagnetism, this gives a single equation involving the known radial magnetic field and its secular variation in two unknown flow components, leading to a severe problem of non-uniqueness. Despite this, we have two specific pieces of flow information which can be deduced directly from the frozen-flux induction equation: the component of flow perpendicular to null-flux curves, contours on which the radial magnetic field vanishes, and the amount of horizontal convergence and divergence at local extrema (maxima, minima and saddle points) of the radial magnetic field. To produce global velocity maps, we make additional assumptions about the nature of the flow and invert the radial induction equation for flow coefficients. However, it is not clear a priori that the flows thus generated are consistent with what we know about them along null-flux curves and at local extrema. This paper examines that issue. We look at typical differences between the null-flux curve perpendicular flow component, and convergence and divergence values at extrema, deduced directly from the induction equation and those from the inversions, investigate the effect of forcing the inversions to produce the correct null-flux curve and extremal values, and characterise the uncertainties on the various quantities contributing. Although the differences between the flow values from the induction equation directly and obtained by inversion seem large, and imposing the direct flow information as side constraints during inversion alters the flows significantly, we also show that these differences are within the likely uncertainties. Thus, we conclude that flows obtained through inversion do not contravene the specific flow information obtained directly from the radial induction equation in the frozen-flux limit. This result should reassure the community that frozen-flux flow inversion is a consistent process, even if including the extremal-value and null-flux conditions as additional information on flow inversion is unlikely to be useful. Solving for a time-dependent core-mantle boundary field model and flow simultaneously may be a good way to produce a temporally-varying field model consistent with the frozen-flux constraint; the ability to fit the data with such a model could be used to establish the timescale over which the frozen-flux assumption is valid.

Key words: Core surface flow modelling, frozen flux hypothesis.

1. Introduction

Deducing the flow at the core-mantle boundary (CMB) from geomagnetic observations suffers from several problems. To make progress, we first make the frozen-flux approximation, whereby magnetic field lines are tied to fluid parcels at the CMB (Roberts and Scott, 1965; Backus, 1968). The jump in electrical conductivity across the CMB means that only the radial component of the magnetic field is guaranteed continuous across this boundary, and therefore we can only glean velocity information from this component of the induction equation. This is a single equation in two unknowns, the tangential flow components (there is no flow across the solid CMB). The exact form of the non-uniqueness was well-characterised by Backus (1968), who showed that only the component of flow perpendicular to null-flux curves (contours on which the radial component of the magnetic field, B_r, vanishes) is uniquely determined. We can also determine the amount of horizontal convergence and divergence at local extrema (maxima, minima and saddle points) of B_r (Whaler, 1980; Benton, 1981). Several non-uniqueness-reducing assumptions have been proposed (e.g., Whaler, 1980; Gubbins, 1982; Le Mouël *et al.*, 1985; Voorhies and Backus, 1985; Holme and Whaler, 2001; Amit and Olson, 2004). We can test whether the assumptions (and frozen-flux) are consistent with the geomagnetic data, which depends on the assumed uncertainties in the geomagnetic field and its secular variation (SV) at the CMB (e.g., Bloxham and Jackson, 1991). It is also possible to characterise mathematically the extent to which the assumptions succeed in reducing the non-uniqueness. We work with spherical harmonic, or Gauss, coefficients of the geomagnetic field and its SV, and their associated standard deviations (neglecting off-diagonal elements of the covariance matrix), treating the SV model coefficients as 'data'. The usual approach taken to estimating the velocity is to solve an over-determined least squares

system with an additional spatial (and possibly temporal) smoothness, or minimum complexity, requirement imposed on the flow, which eliminates the practical non-uniqueness. The question then arises as to whether the flows resulting from damped least squares inversion satisfy the fundamental relationships derivable from the frozen-flux assumption, and further, whether such constraints could be applied directly to help constrain models of core flow. We examine this by two methods: first, we assess the extent to which imposing the constraints based on the fundamental relationships during inversion changes the flows deduced and the fit to the data, and second, estimate the uncertainties on the quantities involved to characterise how serious is the failure of unconstrained flows to satisfy the constraints exactly.

There is a philosophical difficulty with this approach to determining whether flows obtained by inversion are consistent with the frozen-flux hypothesis. The constraints frozen-flux imposes apply at points on the CMB, either along null-flux curves, or at local extrema, and involve pointwise estimates of certain quantities. The true uncertainty on any quantity estimated at a point on the CMB is infinite (e.g., Backus, 1989); what we can calculate is the uncertainty if the quantity was a finite sum of spherical harmonic coefficients, whereas the actual expression is an infinite spherical harmonic sum. We see a practical expression of this below, when the uncertainty increases rapidly as the truncation level of the spherical harmonic expression changes from degree and order 10 to 14. However, we can bound uncertainties on local averages of quantities. We thus justify our approach by noting that imposing smoothness during inversion means that quantities vary slowly spatially, so we regard point values and local averages and, more importantly, their uncertainties, as synonymous. This applies to both the temporally varying magnetic field and the flow at the CMB.

2. Methodology

The radial component of the frozen-flux form of the induction equation at the CMB is

$$\dot{B}_r + B_r \nabla_H . \mathbf{v} + \mathbf{v} . \nabla_H B_r = 0, \tag{1}$$

where B_r is the radial component of the magnetic field, the overdot denotes (partial) time derivative, $\mathbf{v}$ is the tangential velocity and

$$\nabla_H = \hat{\boldsymbol{\theta}} \frac{1}{r} \frac{\partial}{\partial \theta} + \hat{\boldsymbol{\phi}} \frac{1}{r \sin\theta} \frac{\partial}{\partial \phi},$$

working in spherical polar coordinates (r, θ, ϕ). Expanding B_r, $\dot{B}_r$ and toroidal and poloidal scalars representing $\mathbf{v}$ as truncated spherical harmonic series, this can be written (after some algebra) as

$$\dot{\mathbf{g}} = (\mathbf{E}(\mathbf{g}) : \mathbf{G}(\mathbf{g})) \begin{pmatrix} \mathbf{t} \\ \dots \\ \mathbf{s} \end{pmatrix}, \tag{2}$$

where $\dot{\mathbf{g}}$ is a vector of spherical harmonic coefficients of the SV, $\mathbf{E}$ and $\mathbf{G}$ are matrices whose elements are linear combinations of spherical harmonic coefficients of the main field (forming a vector $\mathbf{g}$) multiplying Elsasser and Gaunt integrals respectively, and $\mathbf{t}$ and $\mathbf{s}$ are vectors of spherical harmonic coefficients of the toroidal and poloidal scalars of the flow respectively (see, e.g., Whaler, 1986). Equation (2) is usually solved for $\mathbf{t}$ and $\mathbf{s}$ by least squares inversion. Often, the inversion is damped to minimise the spatial complexity of the flow as well as the misfit to the SV coefficients. In addition, extra non-uniqueness reducing assumptions can be introduced at this point, for instance by combining equations of the form (2) from several epochs to calculate a steady flow, or incorporating a side constraint that imposes tangential geostrophy on the flow. Both the main field and SV coefficients are subject to uncertainties. Standard deviations on the SV are often used to weight the inversion; those on the main field, which are proportionally smaller, are usually ignored (but see Jackson, 1995; Mosegaard and Rygaard-Hjalsted, 1999). Whether or not the inversion is weighted by the SV standard deviations, statistical uncertainties can be placed on the velocity coefficients. For example, Bloxham (1989) plots a CMB flow map with error ellipses derived from the covariance matrix of the flow coefficients.

Here, we wish to test whether these inversion-derived flows are consistent with the flow information deduced directly from the frozen-flux induction equation (1). $\nabla_H . \mathbf{v}$ is a measure of the amount of horizontal convergence or divergence of fluid at the CMB and, for an incompressible flow, the amount of upwelling or downwelling. At local extrema of B_r, i.e. where its horizontal gradient vanishes, we see from (1) that

$$\nabla_H . \mathbf{v} = -\frac{\dot{B}_r}{B_r}, \tag{3}$$

which can be compared with its value from a flow inversion, taking into account the various sources of uncertainty. The positions of the extrema are themselves uncertain, but this uncertainty can easily be estimated in the root-mean-square (rms) sense from the standard deviations of the Gauss coefficients. It is even more straightforward to derive rms uncertainty estimates for B_r and $\dot{B}_r$ and hence to examine whether the convergence and divergence values deduced from an inversion of (2) conform to frozen-flux.

Examining pointwise estimates of the component of flow perpendicular to null-flux curves is more problematical. From (1), with $B_r = 0$,

$$v_\perp = -\frac{\dot{B}_r}{|\nabla_H B_r|}, \tag{4}$$

where $v_\perp$ is the component of $\mathbf{v}$ perpendicular to the null-flux curve. We can only ever examine the flow at a finite set of null-flux curve points, and need to ensure that they are representative. We must also be aware that small changes in the CMB magnetic field, such as would be consistent with its uncertainty, will alter both the position of the null-flux curves and the direction of the normal to it. Besides these sources of uncertainty, there are those on the quantities in (4), from which we calculate uncertainties in both the direction of the normal and the magnitude of the component in that direction. These cannot easily be calculated in a rms sense, so we use standard deviations on the Gauss

coefficients to calculate pointwise uncertainties on the flow components. These are then compared with the component of the flow from a velocity inversion in a range of directions corresponding to the uncertainty in the direction of the normal. We should also compare flow components for a range of positions through which the null-flux curve could pass, given its uncertainties. However, the spatial smoothness constraint on the inversion means that the flow varies slowly, and so we take the standard deviation on its magnitude to be representative of this source of uncertainty, bearing in mind that the actual uncertainties will be a little larger due to this unaccounted-for error.

The convergence and divergence, and the perpendicular velocity component, can both be expressed as linear combinations of the flow coefficients. Thus we can treat the values deduced from both (3) and (4) as additional 'data' during inversion, either separately or jointly. We control the extent to which they are satisfied by a Lagrange multiplier, in much the same way as the smoothness constraint is incorporated. Thus in this case our objective function contains three terms, all quadratic norms of the flow coefficients: one measuring the fit to the SV coefficients, one the smoothness of the flow, and one the fit to the frozen-flux constraints on the flow. Their relative importance during least squares minimisation is controlled by two free parameters.

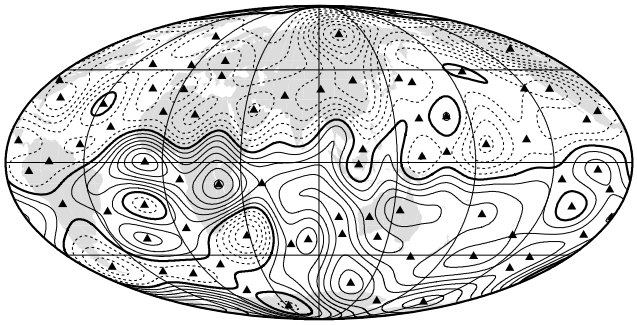

Fig. 1. Contour plot of B_r at the CMB (continent outlines on this and subsequent plots shown for reference) from ufm for 1980. Thick lines are the null-flux curves, positive values are solid, negative values dashed. Contour interval is 0.1 mT. Triangles mark positions of extrema.

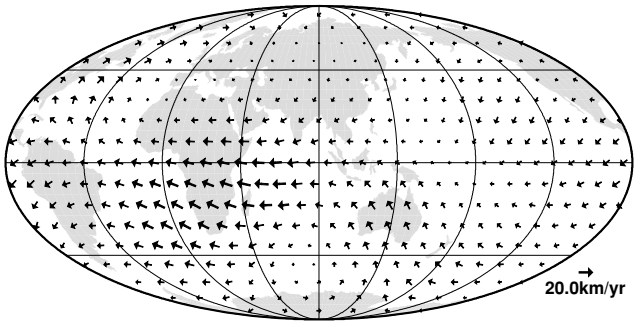

Fig. 2. Steady flow at the CMB from ufm for 1970–80, using main field and SV coefficients for 1970, 1975 and 1980.

3. Data and Results

We use the ufm model of Bloxham and Jackson (1992) which covers the period 1840–1990, although we restrict the analysis here to 1970–80. This is because we seek epochs for which the models are constrained by satellite data, thereby maximising the spherical harmonic degree at which we have useful information, and avoid the end effects present in the last few years of the model. Contours of the 1980 epoch CMB radial field component and its extremal points are shown in Fig. 1. Note that ufm was not constrained to be consistent with frozen-flux. The velocity inversion takes model coefficients from epochs 1970, 1975 and 1980 to determine a steady flow, minimising the spatial complexity norm of Bloxham (1988). To ensure that our conclusions are not specific to steady flows, we also invert for a tangentially geostrophic flow for epoch 1980, which we construct by regularisation of the non-geostrophic flow, using an additional Lagrange multiplier (see, e.g., Holme, 1998). We limit the spherical harmonic degree and order of the analysis to 14; the spatial norm ensures that the flow has converged. Our preferred steady flow is plotted in Fig. 2. It shares features common to most other published flow maps, such as an equatorial band of westward drift beneath the hemisphere centred on the Greenwich meridian, a gyre beneath the southern Indian Ocean and slower flow beneath much of the Pacific hemisphere (e.g., Bloxham and Jackson, 1991; Holme, 2007, and references therein).

There are 71, 74 and 77 extrema of B_r for epochs 1970, 1975 and 1980 respectively. As Fig. 1 shows, many of these are poorly constrained, i.e. a small change to the geometry of the field would cause them to move a significant distance (or even disappear and new ones appear), which we will see later reflected in the large uncertainties in their position. We calculate $\nabla_H.\mathbf{v}$ at these points from the velocity inversion and using (3). We then choose approximately the same number of points along the null-flux curves at each epoch and calculate their $v_\perp$ values from the velocity inversion and using (4). Neither the $\nabla_H.\mathbf{v}$ nor the $v_\perp$ values from the inversion match their values determined directly. A robust way to estimate the differences in the $\nabla_H.\mathbf{v}$ values is to compare $B_r\nabla_H.\mathbf{v}$ with $\dot{B}_r$; the result is given in Table 1. This compares the rms values of the ufm $\dot{B}_r$, their values predicted by the flow inversions (a measure of the goodness-of-fit of the model to the SV data) and the differences between $\dot{B}_r$ and $B_r\nabla_H.\mathbf{v}$, at the extrema of B_r, for 1970, 1975 and 1980. The SV predicted by the steady flow is of the correct order of magnitude, but that predicted by the tangentially geostrophic flow is much less than the actual values at the extrema. However, the normalised rms misfits (last pair of columns) for the tangentially geostrophic flows are smaller than for the steady flows. Table 2 shows the rms value of $v_\perp$ according to (4), the value from the flow inversions and the differences between the two at the digitised points along the null-flux curves. Tables 1 and 2 show that the differences between the estimates of the quantities directly from the induction equation and from the flow inversions are as great as (or greater than) the quantities themselves, regardless of whether the flow is assumed steady or tangentially geostrophic. This suggests that flows obtained by inversion are not compatible with the underlying assumption of frozen flux. Note that the normalised differences in the last pair of columns of Tables 1 and 2, which compare the data

Table 1. Comparison between rms values of $B_r \nabla_H .\mathbf{v}$ and $\dot{B}_r$ (in nT/yr) at the extrema of B_r for the three epochs used to generate a steady flow, and for the 1980 tangentially geostrophic flow. For the first three rows, the second column gives the actual rms $\dot{B}_r$ values from the induction equation, and the following columns, the comparisons with predictions of $\dot{B}_r$ from convergence and divergence of steady flows obtained with two damping parameters, in terms of rms $\dot{B}_r$ values themselves, the rms difference between $\dot{B}_r$ values, and the rms value of the ratio of the difference to $\dot{B}_r$ itself. The left hand set of columns is for a damping parameter of 5×10^{-5}, the right hand set for a damping parameter of 10^{-4}. The final row tabulates the same quantities for 1980 tangentially geostrophic flows, with the left hand column for a damping parameter of 10^{-3}, the right hand column for a damping parameter of 10^{-5}.

Epoch	Actual $(\dot{B}_r)_{\rm rms}$	Predicted $(\dot{B}_r)_{\rm rms}$		$(\delta \dot{B}_r)_{\rm rms}$		$(\delta \dot{B}_r / \dot{B}_r)_{\rm rms}$	
1970	1765	1931	1596	2132	1937	16.5	15.0
1975	1843	1915	1581	2237	2034	141.3	228.0
1980	1878	1915	1584	2317	2102	19.7	21.8
1980G	1878	119	236	1872	1861	1.43	1.25

Table 2. Comparison between rms values of $v_\perp$ (in km/yr) on null-flux curves. As in Table 1, we show the rms values, the rms difference and the rms ratio. The top three rows are for steady flows with damping parameters 5×10^{-5} (left column) and 10^{-5} (right column). The last row is for tangentially geostrophic flows for epoch 1980 with damping parameters 10^{-3} (left column) and 10^{-5} (right column). Note that flows obtained with a smaller damping parameter bring the perpendicular flow components into better agreement with values obtained from the frozen-flux induction equation, whereas flows with heavier damping predict $\dot{B}_r$ more accurately from the convergence and divergence values at extrema of B_r.

Epoch	direct $v_{\rm rms}$	inversion $v_{\rm rms}$		$\delta v_{\rm rms}$		$(\delta v/v)_{\rm rms}$	
1970	9.1	7.4	13.7	9.8	14.9	10.4	7.4
1975	8.6	7.7	14.2	9.4	15.0	7.1	10.0
1980	7.1	7.8	14.2	8.1	14.1	6.9	16.0
1980G	7.1	7.7	15.6	8.6	16.1	20.4	32.2

Table 3. Sum of squares of residuals, SSR (nT^2), flow complexity (in 10^3 $(km/yr)^2$), and rms flow speed (km/yr) for the unconstrained flow, and flows when constraints (3) and (4) are satisfied at the 90% level. SSR reflects only the misfit to the SV coefficients, i.e. does not include the misfit to the constraints that have been included as extra 'data'.

Flow	SSR	Flow complexity	$v_{\rm rms}$
Unconstrained	223.7	74.8	9.6
Extremal constrained	3430	33910	25.9
Null-flux curve constrained	6712	9539	14.8

and model predictions at specific points, are much greater than one (except for the predictions of $\dot{B}_r$ at extrema by the tangentially geostrophic flow), whereas the overall normalised misfits of the inversion flows are much lower—the flows are a reasonable fit to the SV data.

How serious is this incompatibility? It is possible that a small change to the flow pattern would bring it into agreement with the frozen-flux constraints, in which case, we would not regard the apparent failures indicated by Tables 1 and 2 as a cause for concern. To test this, we introduce the constraints given by (3) and (4) by treating them as additional data during inversion, thus also minimising the sums of squares of the differences between the quantities predicted by the flow and those deduced directly from the data. We control how closely we wish them to be satisfied using a Lagrange multiplier. Although (3) only involves the poloidal flow coefficients, inverting for a flow that satisfies the convergence and divergence constraints also alters the toroidal ingredient of the flow. Just as we compare quantities with the dimensions of SV in Table 1, we multiply by the denominators of the right-hand sides of (3) and (4) and treat them as providing additional SV data values at extremal or null-flux curve points, respectively. When imposing (4), we apply it at the same set of null-flux curve points we used to test compatibility. Table 3 summarises the results when we require the constraints to be satisfied at the 90% level. Note that the fit to the data is considerably degraded, and the complexity of the flow is increased, to accommodate the constraints. In fact, the flows are barely converged, due to the increased power in the short spatial wavelength components. Figures 3 and 4 plot the flows for which the null-flux curve and extremal constraints are satisfied (at the 90% level), respectively. The main features of Fig. 2 can still be seen, but superimposed is the small-scale structure necessary to satisfy the constraints, with the modifications concentrated near the null-flux curves or extrema of B_r, but necessarily affecting the flows globally due to the use of spherical harmonics as basis functions.

We also produced flows in which both constraints (3) and (4) have been imposed simultaneously. This turned out to be significantly more difficult than to satisfy either set of constraints separately. The reason why is illustrated by considering the small null-flux patch beneath the North Atlantic. Both B_r and $\dot{B}_r$ are positive within the patch, indicating from (3) that there is convergence; however, on the null-flux curve bounding the patch, because $\dot{B}_r$ is positive, from (4) the flow is anti-parallel to $\nabla_H B_r$, i.e. outward, implying divergence. Thus, to satisfy both sets of constraints simultaneously, the sign of $\nabla_H .\mathbf{v}$ must reverse twice within a very small distance; this is incompatible with the assumption of large-scale flow. However, it is clear that the problem disappears if the sign of $\dot{B}_r$ changes within the patch; since the zero contour of $\dot{B}_r$ lies just to the east of the patch, it is possible that its sign is not robust everywhere within it. This suggests we quantify the uncertainties on the terms appearing in (3) and (4).

The rms uncertainty on $\dot{B}_r$ is strongly dependent on the truncation level of the spherical harmonic series. Expanding to degree and order 10, the standard deviation is

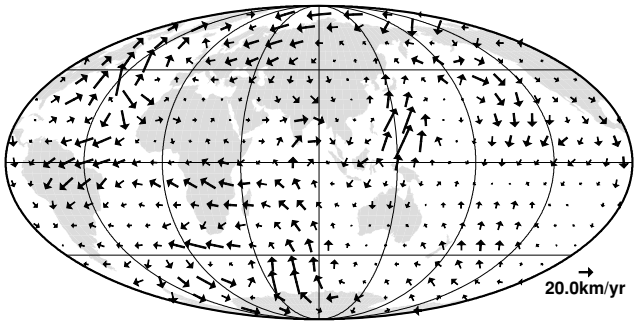

Fig. 3. Steady CMB flow matching values of the flow speed normal to null-flux curves.

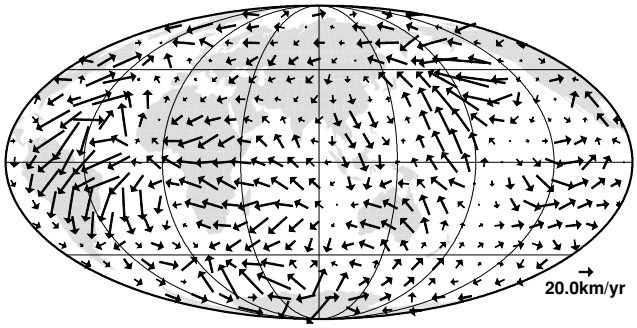

Fig. 4. Steady CMB flow matching values of convergence and divergence at extrema of B_r.

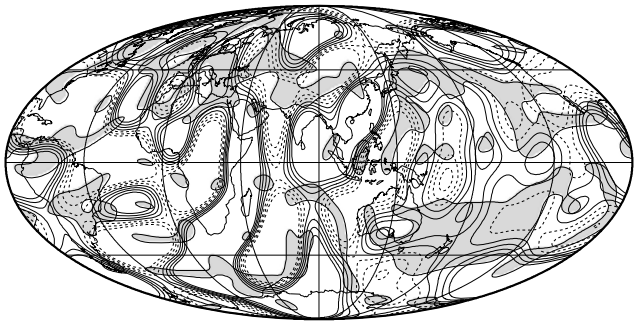

Fig. 5. Contours of the difference between $\dot{B}_r$ and $B_r \nabla_H .\mathbf{v}$, at 500 nT/yr intervals up to $\pm$1500 nT/yr (a representative standard deviation of $\dot{B}_r$), with negative values dashed. The grey shaded areas are where $|\nabla_H B_r|$ is zero to within one standard deviation. Since $\dot{B}_r$ should equal $B_r \nabla_H .\mathbf{v}$ where $|\nabla_H B_r|$ vanishes, the grey areas should be intersected by contours of $\dot{B}_r - B_r \nabla_H .\mathbf{v}$ in the range shown. The epoch is 1980, but the picture is similar for 1970 and 1975.

1381 nT/yr, rising rapidly to 17493 nT/yr for degree 14 (which implies $\dot{B}_r$ is zero to within less than half a standard deviation everywhere on the CMB!). We will take 1500 nT/yr to be an indicative estimate, from which it can be seen that the incompatibility between the two sets of constraints discussed in the previous paragraph is more apparent than real: since $\dot{B}_r$ is 2951 nT/yr at the North Atlantic extremum of B_r (in 1970; values for the other two epochs are similar), a change of sign is within 2 standard deviations. We can also calculate an rms uncertainty on the horizontal gradient of B_r, 207 nT/km including terms up to degree and order 14, which is less sensitive to truncation level than the SV, but more so than B_r itself, since the gradient operator preferentially amplifies the less well constrained shorter wavelengths. Figure 5 shows the result of superimposing the two sources of uncertainty for 1980. $|\nabla_H B_r|$ is zero to within one standard deviation anywhere within the grey shaded areas, many of which are quite large and frequently contain more than one extremum (compare with Fig. 1). This illustrates how poorly constrained many extrema are, lying in areas of the CMB where B_r is almost flat. The contours are of the difference between $\dot{B}_r$ and $B_r \nabla_H .\mathbf{v}$, at 500 nT/yr intervals up to $\pm$1500 nT/yr, with negative values dashed. Thus, where these bands intersect a grey shaded area, the constraint of (3) is satisfied at the extremum (or extrema) enclosed to within approximately one standard deviation (depending on the spherical harmonic truncation level chosen). There are only 5 grey shaded patches inside which $\dot{B}_r - B_r \nabla_H .\mathbf{v}$ exceeds $\pm$1500 nT/yr (i.e. the patches are not intersected by the contours in Fig. 5), and one of these (the patch beneath Thailand and the south-east Indian ocean) does not contain an extremum—although both horizontal derivatives of B_r vanish, their zero contours do not quite intersect. Thus the constraint fails at the one standard deviation level at only 4 out of 77 extrema, well below the one-third to be expected by chance. Hence we deduce that flow inversions satisfy the constraint on convergence and divergence deduced from frozen-flux.

As noted earlier, many of the extrema are poorly constrained, lying in areas of the core where B_r is almost flat. H. Amit (2007, pers. comm.) has pointed out that at many of them, particularly those beneath the Pacific, B_r and $\dot{B}_r$ are both small, so the inverted flow and its upwelling and downwelling are weak, and hence the fit to the frozen-flux constraints is good. He suggested that a more robust test of the frozen-flux constraints would be to examine only well-defined extrema, defined by those contained within small grey patches in Fig. 5 where the B_r values are large. He notes that it is the displacement of these intense magnetic field features that should constrain core flow models. The decision as to which extrema should be included in this set is somewhat subjective, but we chose only those easily identified at all three epochs, inside grey patches enclosing a single extremum, and for which the B_r values were significantly non-zero. This gave 11 extrema, all but two of which were outside the area of low SV beneath the Pacific. For 1980, at 6 of them, (3) is satisfied to within 1 standard deviation; at a further 3, within 2 standard deviations; and the final 2 are satisfied to between 2 and 3 standard deviations. This is a good approximation to the expected Gaussian distribution (for a small number of samples). Thus the inversion flows appear to be consistent with frozen-flux. It is also very easy to invert for a flow satisfying the constraints, although this is mainly because they provide only 11 extra 'data' points.

In Fig. 6, we plot the pointwise upwelling and downwelling values for 1980 from (3) (results from other epochs are similar) and contour values from a flow inversion. This allows a qualitative, visual comparison between the two types of upwelling estimate, to complement the quantitative comparison of Table 1. The agreement between the two is fair, both in magnitude and sign, for the small-to-

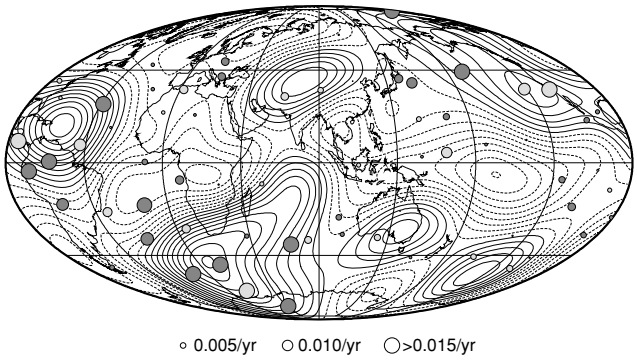

Fig. 6. Contours of upwelling from steady flow shown in Fig. 1. Contour interval is 0.001/yr; negative values are dashed. Superimposed are the pointwise values from (3) for 1980, with the size of the circle reflecting the amplitude, dark grey shaded for positive values, light grey shaded for negative values.

moderate pointwise values. For example, several of the very small pointwise values—some of which are invisible at the scale chosen here, but their positions can be identified from Fig. 1—lie close to zero upwelling contours. The unfeasibly large (up to two orders of magnitude greater than values obtained from inversion) pointwise upwelling and downwelling values obtained from (3) are the consequence of non-zero $\dot{B}_r$ where B_r is small. Backus (1968) refers to points where both B_r and its horizontal divergence vanish as double null-flux points, and points out that they must have zero $\dot{B}_r$ to be consistent with frozen-flux. To within one standard deviation in B_r (approximately 0.05 mT to degree and order 14), 7 of the extrema in Fig. 1 could be double null-flux points; at 3 of them, $\dot{B}_r$ is zero to within one standard deviation, and at 5, zero to within two standard deviations, fewer than would be expected statistically for consistency with frozen flux. However, when the uncertainty in the locations of the extrema is taken into account as well, the condition is satisfied at 6 out of the 7 points. Formally, upwelling/downwelling is not defined at double null-flux points, so we should not be too concerned by the large values at these 7 extrema. One of them is the extremum in the small null-flux patch beneath the North Atlantic discussed earlier. Examining a longer time period than that considered here, Gubbins (2007) argues that the changes in flux through some southern hemisphere null-flux patches over the 20th century have been as large as the changes in flux through patches bounded by non-zero contours of B_r used to estimate upwelling (Whaler, 1984), and therefore that the SV changes could be as easily ascribed to flux expulsion by upwelling (a diffusive process). Tangentially geostrophic upwelling and downwelling is largest near the equator, and upwelling is associated with equatorward flow, downwelling with poleward flow (Gire and Le Mouël, 1990). As Figs. 2 and 6 show, our pointwise values, and the steady flow inversion results, do not follow the same pattern.

To examine the uncertainties on flow on null-flux curves, we begin by estimating the uncertainty in the direction of the normal to the null-flux curve, i.e. the direction of $\nabla_H B_r$, at any point. Let the angle the direction of $\nabla_H B_r$ makes with North be α, so that

$$\tan\alpha = \frac{(\nabla_H B_r)_\phi}{(\nabla_H B_r)_\theta} = \frac{1}{\sin\theta}\frac{\partial B_r}{\partial\phi}\Big/\frac{\partial B_r}{\partial\theta} \equiv \frac{x}{y}.$$

The rms uncertainty on α cannot be calculated in a straightforward fashion, so instead we estimate its standard deviation at individual points along null-flux curves. This is more numerical effort than estimating an rms value, but is scientifically more rigorous. Defining σ_x^2 as the variance of x and σ_{xy}^2 as the covariance between x and y, the variance of α is given by

$$\sigma_\alpha^2 = \frac{y^2\sigma_x^2 + x^2\sigma_y^2 - 2xy\sigma_{xy}^2}{(x^2+y^2)^2}. \qquad (5)$$

Here, the functions x and y, and hence their variances and covariances, are functions of the Gauss coefficients, which are themselves correlated. We discuss the implications of this for estimates of the uncertainty in α, and give numerical values, in Appendix. The standard deviation of $v_\perp$ is

$$\sigma_{v_\perp} = \frac{1}{|\nabla_H B_r|}\sqrt{\sigma_{\dot{B}_r}^2 + \left(\frac{\dot{B}_r}{|\nabla_H B_r|}\right)^2 \sigma_{|\nabla_H B_r|}^2}\ , \qquad (6)$$

involving the variances of the radial SV and $\nabla_H B_r$, as well as the quantities themselves.

Independently, we can also calculate the covariance matrices for the flows obtained through inversion, which define error ellipses on the flow vectors (e.g., Bloxham, 1989). These are different for the unconstrained and the two constrained flows, even though the damping parameter controlling spatial complexity is the same in all three cases, since we treat the constraints as extra data (Bloxham *et al.*, 1989, see equations (3.13)–(3.15)). We use them to calculate the standard deviations on the components of flow in the direction of the normal to the null-flux curve. There is an additional source of uncertainty in this flow component, however, since the direction of the normal along which we calculate it is also uncertain, as expressed through the angle variance σ_α^2 given by (5) and tabulated in Appendix. We have therefore varied α by up to $\pm\sigma_\alpha$ and found the maximum and minimum flow component values within that swathe of possible directions to the normal. In most cases, the extremal values are found at the ends of the range of possible directions; when they lie within the range of angles, we have ensured that we are allowing the direction to vary finely enough to capture the maximum and minimum values. In some cases, varying α encompasses only a small range of flow component values. In others, usually when the direction of α is poorly defined (but occasionally when the flow uncertainty is large at the point), varying it within $\pm\sigma_\alpha$ allows a huge range of flow components. The results for 1980 are shown in Table 4 (those from the other two epochs used to calculate the steady flow are similar). The first column is $v_\perp$, the second column its value from the inverse steady flow, and the third and fourth, the range of flow component values as α is varied. Columns 5–7 are the same quantities for the flow for which the constraints (3) have been imposed, and columns 8–10 for the flow for which the constraints (4) have been imposed. Standard deviations on the inverse $v_\perp$ estimates are denoted with subscripts u, e

Table 4. Flow components perpendicular to null-flux curves for 1980. The first column is deduced directly from the induction equation, with its one standard deviation $\sigma_{v_\perp}$ from (6). The second column is computed from the damped least squares inversion flow, with its standard deviation σ_u from the flow coefficients covariance matrix. The third and fourth columns are the minimum and maximum values calculated from the damped inverse flow when α is allowed to vary within one standard deviation; this indicates the variability resulting from this additional source of uncertainty. Columns 5–7 tabulate the same quantities for the flow constrained to satisfy the conditions (3) at extrema of B_r, with standard deviation σ_e, and columns 8–10, for the flows constrained to satisfy conditions (4) on null-flux curves, with standard deviation σ_n. All values are in km/yr.

direct	unconstrained			extremal points constrained			null-flux curves constrained		
$v_\perp \pm \sigma_{v_\perp}$	$v_\perp \pm \sigma_u$	minimum	maximum	$v_\perp \pm \sigma_e$	minimum	maximum	$v_\perp \pm \sigma_n$	minimum	maximum
−5.9±3.4	−4.2±0.7	−5.2	−2.9	−6.0±4.5	−12.7	1.2	−5.4±0.3	−11.0	0.6
−6.5±4.1	−0.7±0.7	−2.3	1.0	−12.4±3.9	−13.4	−10.4	−6.3±0.3	−9.8	−2.3
−1.1±3.7	0.7±0.5	−0.9	2.4	14.2±3.0	18.8	9.0	0.3±0.2	−2.0	2.6
−2.9±5.2	−6.3±0.9	−7.0	−4.3	5.8±6.1	−8.1	18.4	−1.7±0.3	−16.0	12.9
2.4±20.2	−5.5±1.5	−2.5	5.1	−56.5±7.1	−62.4	39.5	−1.5±0.5	−17.3	18.0
−11.4±42.1	6.4±1.3	−6.5	7.3	58.9±7.3	−47.9	61.9	−14.6±0.5	−25.7	25.9
−14.6±9.6	−6.0±1.2	−9.0	−2.0	55.5±6.9	70.3	31.4	−15.6±0.4	−18.5	−10.1
−5.4±6.2	6.5±1.1	1.9	8.3	−16.2±6.4	−39.9	14.6	−7.4±0.4	−13.5	1.9
1.4±4.4	2.8±0.8	0.3	4.8	−46.5±4.0	−47.1	−39.4	1.5±0.2	1.4	1.5
1.3±7.4	−3.7±1.4	−4.7	−0.7	−4.6±8.4	18.8	−25.5	1.3±0.4	−6.7	8.6
−1.2±3.2	1.0±1.3	1.3	3.2	31.9±8.1	22.5	38.0	−1.2±0.3	−2.9	0.6
0.6±4.3	0.1±0.4	−2.7	2.9	15.2±2.3	11.6	16.3	0.9±0.1	−0.5	2.3
−0.2±5.6	−1.6±0.8	−6.1	3.5	23.3±5.2	7.0	32.2	0.3±0.3	−7.3	7.8
−1.3±3.5	0.5±0.7	−2.6	3.6	9.4±4.4	−1.9	19.5	−0.8±0.2	−5.7	4.2
12.6±13.8	10.7±0.7	5.3	11.2	3.3±4.4	−1.1	6.2	12.9±0.2	2.8	17.0
6.1±4.0	12.4±0.8	10.8	12.8	2.7±4.7	0.0	5.2	6.2±0.3	3.7	8.1
−1.1±4.6	−3.8±0.8	−8.1	1.3	1.8±4.4	−17.1	20.4	−0.5±0.2	−10.8	9.9
−6.6±3.3	−6.8±0.7	−8.4	−4.8	2.5±3.9	−9.4	14.3	−6.6±0.2	−12.3	−0.5
−4.0±2.5	−8.4±0.9	−9.1	−7.2	−28.8±5.4	−32.7	−23.6	−4.0±0.2	−8.1	0.2
0.0±1.8	0.1±0.2	−1.3	1.5	−3.7±1.5	−4.3	−3.0	0.0±0.1	−0.9	0.9
2.9±1.6	4.9±0.7	3.3	6.3	10.1±4.4	6.7	13.2	2.8±0.2	2.0	3.6
−2.9±2.0	−8.3±0.8	−10.0	−6.3	−8.6±5.7	−14.8	−2.2	−3.0±0.3	−3.0	−2.9
3.7±2.1	8.7±0.8	6.5	10.6	18.9±5.8	16.2	21.0	3.7±0.3	3.1	4.2
6.7±3.3	2.4±0.2	−1.2	6.0	−1.0±1.6	−6.3	4.2	6.7±0.1	6.5	6.7
7.7±4.2	−3.4±0.6	−6.0	−0.4	−10.3±4.1	−11.3	−8.5	7.7±0.3	2.2	12.7
3.0±2.7	4.8±0.3	3.3	6.0	16.8±1.9	12.6	20.0	3.1±0.1	2.4	3.7
6.0±5.4	8.3±1.1	7.4	8.3	−16.2±7.1	−6.1	−23.0	5.9±0.4	0.6	10.1
5.2±5.1	9.6±1.1	8.3	9.6	−11.6±7.0	−16.8	−4.1	5.2±0.4	−1.0	10.4
−9.4±7.5	−9.7±1.1	−9.5	−7.8	12.4±7.0	1.0	20.9	−9.3±0.3	−13.7	−2.8
−10.8±9.4	−7.8±1.0	−7.9	−6.1	18.4±6.3	8.4	22.9	−12.3±0.3	−12.4	−10.1
−15.6±17.5	−2.5±0.6	−4.8	1.1	7.9±4.0	8.0	3.8	−16.5±0.2	−42.0	17.4
−14.3±19.2	3.8±1.2	0.7	4.4	2.7±7.2	−2.7	6.0	−14.2±0.3	−46.6	29.0
−8.4±6.2	5.7±1.2	4.9	5.7	2.3±6.7	0.0	4.1	−9.3±0.3	−24.7	8.0
−1.3±3.0	0.3±0.9	−2.3	2.7	6.5±5.5	3.5	8.9	−1.4±0.3	−1.8	−0.9
−1.0±2.7	−5.0±0.6	−5.5	−4.2	−22.1±3.9	−23.7	−18.9	−1.2±0.2	−2.1	−0.2
−1.3±2.7	1.3±0.6	0.3	2.2	−5.7±3.6	−11.9	1.0	−1.4±0.2	−1.4	−1.3
−0.9±7.7	5.1±0.9	−1.4	8.8	−19.4±5.5	−28.6	0.6	−0.2±0.3	0.5	−0.8
1.1±4.1	−7.2±0.5	−9.2	−4.2	18.1±3.1	11.6	21.9	1.2±0.2	0.7	1.5
0.8±4.7	−3.8±0.9	−7.1	0.2	12.0±5.7	19.8	1.7	0.7±0.3	0.3	0.9
−0.1±4.9	6.4±0.8	3.2	8.3	−25.5±4.8	−26.1	−19.3	−0.1±0.3	−0.9	0.8
3.2±2.9	9.9±0.5	7.7	11.7	−29.2±2.8	−23.2	−34.3	3.5±0.1	1.7	5.2
1.4±2.0	0.8±0.4	−3.3	4.9	−29.9±2.6	−27.2	−30.8	1.3±0.1	−2.2	4.7
1.7±2.6	−1.3±0.5	−11.6	9.7	38.5±2.8	39.7	22.1	1.7±0.2	−1.5	4.0
−1.1±3.9	−17.4±0.8	−18.2	−12.7	3.8±5.1	−4.3	11.0	−1.5±0.3	−5.6	2.9
9.4±10.9	2.2±1.2	−2.4	6.0	−6.6±6.7	−9.7	−0.8	8.9±0.3	6.1	8.1
8.9±5.7	0.6±1.0	−1.4	2.5	−35.0±5.0	−40.9	−25.1	9.1±0.3	1.9	15.2
3.2±2.8	2.7±1.2	1.1	4.2	17.6±6.3	21.3	12.7	3.5±0.4	−0.7	7.5
6.7±3.8	6.3±1.2	5.8	6.4	−27.7±5.0	−39.1	−14.4	7.0±0.3	4.9	8.7
0.6±5.0	1.9±0.7	−2.7	6.1	−10.1±4.1	0.0	−17.8	1.3±0.2	−1.4	3.7
−7.1±6.9	−9.4±1.2	−9.7	−7.1	−25.6±7.1	−26.4	−19.3	−7.1±0.4	−9.4	−3.3
−7.5±4.5	−4.0±0.7	−7.2	−0.3	−16.4±4.2	−16.3	−14.4	−7.6±0.2	−9.0	−5.2
21.1±20.2	11.9±0.8	6.3	13.1	0.2±4.8	−0.1	0.3	21.1±0.3	11.0	23.3
12.3±6.2	14.9±0.9	12.9	15.4	15.2±6.3	11.2	17.8	12.4±0.3	8.0	15.8
4.7±1.5	10.4±0.5	8.8	11.9	7.0±3.6	9.5	4.4	4.7±0.2	2.9	6.4
−4.9±2.2	−13.2±1.1	−13.2	−12.9	−34.2±7.7	−36.1	−31.2	−4.9±0.4	−6.2	−3.5
−8.2±3.0	−5.8±1.1	−6.7	−4.3	−18.5±6.2	−21.3	−15.1	−8.1±0.4	−9.5	−6.4
−9.8±4.6	1.1±0.8	−1.0	3.0	−25.4±4.0	−30.7	−18.4	−9.8±0.2	−13.2	−5.7
15.2±19.6	−6.1±1.1	−8.5	0.0	−7.6±6.0	−44.9	34.4	15.7±0.3	11.0	15.7
6.2±2.8	4.4±0.8	3.7	4.9	13.0±4.5	11.5	14.0	6.2±0.3	4.8	7.3
3.9±2.7	4.6±1.0	3.6	5.5	−11.4±6.3	−14.2	−8.0	3.8±0.3	3.6	3.8
1.0±2.7	1.9±0.8	−0.2	3.8	−11.0±4.6	−11.0	−10.7	1.1±0.3	0.7	1.4

and n, for unconstrained, extremal points constrained, and null-flux curve constrained, respectively. We have used rms variances of $\dot{B}_r$ and $\nabla_H B_r$ in (6); the results would not differ greatly if we used point-wise values. Imposing the extremal constraints has increased σ_e by a factor of typically 5 (over σ_u), while imposing the null-flux curve constraints has reduced σ_n by about a factor of 3.

Unlike the convergence and divergence values at extrema of B_r, the flows obtained through damped least squares inversion do not immediately appear to be consistent with the constraints on their components normal to null-flux curves. The range of values of the flow component as α is varied encompasses the actual $v_\perp$ value at only 20 (out of 61) null-flux curve points. But this number can be increased to 42, consistent with the two-thirds expected statistically, by accounting for the uncertainties in the direct $v_\perp$ components. In general, their standard deviations $\sigma_{v_\perp}$, calculated from (6), are much larger than those on the inverse $v_\perp$ components, σ_u, calculated from the covariance matrix. This reflects primarily the uncertainty in $\nabla_H B_r$, which also determines the amount of variability in α. Hence Table 4 shows that the range of values of the inverse $v_\perp$ component as α is varied tends to be large when $\sigma_{v_\perp}$ is large, and the range of variability of inverse $v_\perp$ components is typical of $\sigma_{v_\perp}$. Columns 5–7 show that flows constrained to satisfy the constraints (3) at extrema of B_r only match the actual $v_\perp$ values at 18 null-flux curve points (to within one standard deviation on each quantity). As previously noted, matching the constraints at extrema of B_r tends to increase the flow amplitude, so the inverse $v_\perp$ components are typically larger than those obtained in the other calculations. Thus, the inverse flow components at only 6 more null-flux curve points are in agreement with the direct $v_\perp$ values when the variability arising from uncertainty in α is taken into account. This is another illustration of the incompatibility between the constraints. In contrast, the range of values of the $v_\perp$ components from inversions in which the null-flux constraints (4) have been imposed include the direct $v_\perp$ value at all but 5 null-flux curve points, even without accounting for their standard deviations.

4. Discussion

An initial calculation of the differences between direct (from the frozen-flux radial component of the induction equation) and inversion-based flow components perpendicular to null-flux curves, and convergence and divergence at extrema of B_r, suggested that the two sets of values were badly inconsistent. Imposing the constraints during inversion markedly altered the flows and the fit to the SV. However, analysis of the uncertainties demonstrates that most of these differences are well within the errors.

Our study has been conducted using field models constrained primarily with ground data, especially concerning the SV. Current satellite magnetic missions Ørsted and CHAMP have been providing almost global, continuous coverage of the vector magnetic field for a number of years, from which models have been produced which give better estimates of both the shorter wavelength components of the magnetic field and the SV. Unfortunately, it is not yet clear whether such models would provide greater insight for a study of this kind. The SV in the new models is definitely determined far better (at least for the subdecadal period over which the satellites have flown), but its spectrum is "blue": power increases steadily with harmonic degree (Holme and Olsen, 2006). Noise in individual coefficients becomes increasingly a problem with higher degree, to the extent that even simple tests for frozen flux become inconclusive: while it impossible to reject the frozen-flux hypothesis, a more positive test seems increasingly unlikely to be possible. Lack of knowledge of the higher degree components of the main field due to the lithospheric field may be an even greater problem. While the internal field is undoubtedly resolved far better in satellite data models than in models such as ufm, the transition between the core and lithospheric fields is still unclear, and a conservative view would taper such models to give a core field with spectrum little different to that of ufm. The unknown higher-degree field places additional uncertainty on the position of null-flux curves and field extrema. Further, Eymin and Hulot (2005) show, following earlier conjectures of Hulot *et al.* (1992), that the flow can interact with the small scale field to produce low degree secular variation, imposing an additional, perhaps dominant, contribution to the uncertainty in fit to observed SV. While better and better data could in principle allow the accurate determination of higher degree SV, the high-degree field is always likely to be beyond direct observational constraint. The best we can do is probably to accept the lack of precision in the main field, and constrain the secular variation by modelling the field over longer time, as is done with the historical data and the ufm model used here.

The ufm model we used to define the main field and SV for this study is not consistent with frozen-flux. In particular, there was a strong increase in the flux through the patch bounded by the null-flux curve beneath South America, the southern Atlantic Ocean and the south-western part of the Indian Ocean between 1960 and 1980 (Bloxham *et al.*, 1989). Bloxham and Gubbins (1986) produced a series of 'snapshots' of the main field in which flux through patches bounded by null-flux curves was conserved, a necessary condition for the frozen-flux hypothesis to hold. The extension of this concept to produce a continuously time-varying field model consistent with frozen-flux is ongoing; Jackson *et al.* (2007) have developed a new method for implementing this constraint and that imposed by Kelvin's circulation theorem (Jackson, 1996), which they believe offers greater promise for producing a continuously time-varying field model consistent with frozen-flux. However, it remains to be seen how much better flows derived from such a model would satisfy the conditions (3) and (4). Another approach would be to generate a frozen-flux field model and time-dependent core flow model simultaneously, by solving for an initial field, and a time-varying flow which will define the field morphology at later epochs. Such a fully self-consistent approach should ensure that constraints (3) and (4) are satisfied, although because evolution of the field depends on the time-integration of the product of the field and the flow, the inverse problem is significantly non-linear (Voorhies, 1986; Bloxham, 1988). This would also address the question of the existence of a model consistent with

Table 5. $\sigma_x^2, \sigma_y^2, \sigma_{xy}^2$ and σ_α (in degrees), where $x = \frac{1}{\sin\theta}\frac{\partial B_r}{\partial \phi}$ and $y = \frac{\partial B_r}{\partial \theta}$, for 61 points along null-flux curves for epoch 1980, showing that the covariance term is typically 3 orders of magnitude smaller than the variances.

σ_x^2	σ_y^2	σ_{xy}^2	σ_α	σ_x^2	σ_y^2	σ_{xy}^2	σ_α
2.44×10^{11}	2.54×10^{11}	-9.10×10^{7}	14.5	2.49×10^{11}	3.00×10^{11}	-2.05×10^{8}	51.8
2.47×10^{11}	2.52×10^{11}	1.89×10^{9}	16.7	2.53×10^{11}	3.24×10^{11}	2.55×10^{8}	24.9
2.48×10^{11}	2.51×10^{11}	2.26×10^{9}	11.8	2.53×10^{11}	3.27×10^{11}	3.99×10^{7}	17.4
2.46×10^{11}	2.49×10^{11}	-4.43×10^{9}	26.5	2.53×10^{11}	3.25×10^{11}	6.94×10^{8}	15.5
2.48×10^{11}	2.45×10^{11}	2.11×10^{7}	104.0	2.53×10^{11}	3.20×10^{11}	3.59×10^{8}	15.2
2.46×10^{11}	2.46×10^{11}	4.85×10^{8}	122.7	2.50×10^{11}	2.99×10^{11}	3.24×10^{7}	43.9
2.49×10^{11}	2.58×10^{11}	-1.79×10^{8}	23.7	2.51×10^{11}	2.99×10^{11}	-1.24×10^{8}	22.7
2.48×10^{11}	2.71×10^{11}	-1.93×10^{8}	38.6	2.49×10^{11}	2.69×10^{11}	-5.97×10^{7}	26.3
2.50×10^{11}	2.57×10^{11}	-1.26×10^{8}	23.8	2.49×10^{11}	2.70×10^{11}	1.53×10^{7}	27.2
2.53×10^{11}	2.84×10^{11}	-7.74×10^{8}	42.4	2.48×10^{11}	2.96×10^{11}	2.52×10^{7}	10.2
2.52×10^{11}	2.82×10^{11}	-7.48×10^{7}	18.4	2.49×10^{11}	2.98×10^{11}	9.15×10^{8}	13.9
2.53×10^{11}	3.27×10^{11}	-4.14×10^{8}	23.7	2.47×10^{11}	2.70×10^{11}	2.45×10^{8}	41.8
2.50×10^{11}	3.28×10^{11}	2.38×10^{-6}	32.6	2.45×10^{11}	2.70×10^{11}	-4.23×10^{8}	27.3
2.54×10^{11}	3.23×10^{11}	-3.75×10^{8}	19.7	2.48×10^{11}	2.55×10^{11}	-9.94×10^{7}	36.7
2.54×10^{11}	3.22×10^{11}	2.05×10^{8}	39.8	2.49×10^{11}	2.56×10^{11}	-1.04×10^{8}	19.7
2.54×10^{11}	3.12×10^{11}	-1.25×10^{8}	17.7	2.46×10^{11}	2.52×10^{11}	-1.55×10^{9}	14.1
2.53×10^{11}	3.10×10^{11}	-1.64×10^{8}	26.1	2.51×10^{11}	2.49×10^{11}	-1.15×10^{9}	15.2
2.49×10^{11}	3.31×10^{11}	3.25×10^{-6}	12.7	2.51×10^{11}	2.59×10^{11}	-1.32×10^{8}	27.3
2.51×10^{11}	3.13×10^{11}	6.82×10^{8}	12.6	2.51×10^{11}	2.50×10^{11}	1.34×10^{8}	26.9
2.49×10^{11}	2.97×10^{11}	-8.46×10^{8}	9.4	2.51×10^{11}	2.45×10^{11}	-2.86×10^{6}	20.5
2.50×10^{11}	3.13×10^{11}	-8.10×10^{8}	8.5	2.51×10^{11}	2.42×10^{11}	1.50×10^{8}	35.6
2.51×10^{11}	3.09×10^{11}	2.59×10^{8}	10.4	2.49×10^{11}	2.49×10^{11}	-4.05×10^{6}	17.3
2.51×10^{11}	3.15×10^{11}	-5.39×10^{8}	10.7	2.48×10^{11}	2.71×10^{11}	-2.39×10^{8}	6.9
2.54×10^{11}	3.22×10^{11}	2.44×10^{8}	13.2	2.50×10^{11}	2.58×10^{11}	3.23×10^{8}	10.2
2.53×10^{11}	3.11×10^{11}	-3.99×10^{8}	16.3	2.48×10^{11}	2.47×10^{11}	2.73×10^{8}	10.8
2.53×10^{11}	2.84×10^{11}	8.96×10^{7}	13.8	2.49×10^{11}	2.44×10^{11}	6.55×10^{8}	14.9
2.53×10^{11}	3.11×10^{11}	8.95×10^{7}	25.6	2.52×10^{11}	2.43×10^{11}	-5.94×10^{8}	45.8
2.50×10^{11}	3.25×10^{11}	4.65×10^{-6}	25.6	2.57×10^{11}	2.43×10^{11}	6.77×10^{7}	11.5
2.54×10^{11}	3.21×10^{11}	4.23×10^{8}	27.9	2.52×10^{11}	2.42×10^{11}	3.25×10^{8}	12.8
2.54×10^{11}	3.20×10^{11}	2.77×10^{7}	31.8	2.49×10^{11}	2.47×10^{11}	-6.33×10^{7}	14.5
2.50×10^{11}	2.97×10^{11}	1.11×10^{8}	41.4				

frozen-flux (i.e. whether it fits the data adequately), and might also provide constraint on core field above spherical harmonic degree 14, because of its influence in positioning the radial field extrema and null-flux curves.

The method by which we have imposed the constraints indicated by (4) during inversion is similar to that which Wicht and Jault (1999) used to determine the toroidal part of $\mathbf{v}B_r$. They applied (4) at a sequence of points along null-flux curves to give a set of equations of condition for the toroidal flow coefficients, ignoring the equations of condition provided by the frozen-flux form of the radial induction equation (this would be like attaching a very large weight to the constraints of (4) in our calculations, thereby downweighting strongly the information from the induction equation). They showed that the flow so determined is not sensitive to the distribution of the points provided their density is sufficiently high (about 200 points), so long as the flow is regularised in the usual fashion during inversion. This, and the use of spherical harmonics to provide a global set of basis functions, enabled them to extrapolate the toroidal flow component away from null-flux curves. Their resulting flows resemble those found by the traditional inversion method.

In a similar fashion, (3) could be used to define equations of condition for both the toroidal and poloidal flow coefficients. The extrema of B_r are more evenly distributed over the CMB than sets of points defining the null-flux curves, suggesting that the flow so defined would be better determined. However, we have seen how poorly constrained the extremal positions are, and their numbers cannot be increased, unlike points along a null-flux curve, so the least squares problem would be seriously underdetermined. Hence it is unlikely that the extremal constraints on their own would provide a useful practical technique for flow determination. Even more importantly, where their position falls at a point where the magnitude of B_r is low, but the radial SV is not small, then condition (3) requires a flow with unphysically large upwelling. An inversion scheme would need to incorporate constraints limiting the amount of upwelling, unless downweighting such points owing to their large uncertainties and standard methods of flow regularisation were sufficient to give reasonable values. It therefore seems unlikely that conditions at the extremal points, and to a lesser extent, the null-flux curves, can sensibly be built into an inversion scheme, particularly given uncertainties due to the unmodelled high-degree field, and spectrally "blue" secular variation.

Nevertheless, by calculating flow quantities directly from the radial component of the diffusion-less induction equation and comparing them with their counterparts from flows

obtained by inverting SV, we have shown that inversion flows do not contradict the pointwise flow information, once uncertainties are taken into account. Thus regularised flow inversion does not contravene the underlying frozen flux constraints and involves solving a consistent system. Flow inversion tends to match the upwelling and downwelling values at extremal points where the magnitude of B_r is high better than where B_r is small. A few of the extrema where B_r is small could be double null-flux points, at which $\dot{B}_r$ must also be zero to be consistent with frozen-flux (Backus, 1968). As we have seen, small deviations from this constraint give unfeasibly large upwelling that is not reproduced in flow inversions. Thus flow inversion may provide a good way of producing temporally-varying core fields consistent with the frozen-flux hypothesis.

Acknowledgments. This work was begun when KAW was visiting Gauß Professor at the Institut für Geophysik, Universität Göttingen, funded by the Göttingen Academy of Sciences. She is particularly grateful for the hospitality of Karsten Bahr, and useful discussions with Johannes Wicht. It was completed with funding from NERC under grants NER/O/S/2003/00674 and NER/O/S/2003/00675. Thanks to Andrew Jackson for providing the ufm field model covariance matrix. Hagay Amit produced a particularly helpful review of an earlier version of this manuscript, and an anonymous reviewer made some useful points.

Appendix A.

Equation (5) gives the variance of α as

$$\sigma_\alpha^2 = \frac{y^2\sigma_x^2 + x^2\sigma_y^2 - 2xy\sigma_{xy}^2}{(x^2+y^2)^2},$$

where $x = \frac{1}{\sin\theta}\left(\frac{\partial B_r}{\partial \phi}\right)$ and $y = \left(\frac{\partial B_r}{\partial \theta}\right)$, i.e. $x^2 + y^2 = r^2(\nabla_H B_r)^2$. Expanding x and y in terms of the Gauss coefficients, we have

$$\sigma_x^2 = \sum_l \left(\frac{a}{r}\right)^{2l+4} (l+1)^2 \cdot \sum_{m=0}^{l} \left(\frac{dP_l^m}{d\theta}\right)^2 \left(\sigma_{g_l^m}^2 \cos^2 m\phi + \sigma_{h_l^m}^2 \sin^2 m\phi\right),$$

$$\sigma_y^2 = \sum_l \left(\frac{a}{r}\right)^{2l+4} (l+1)^2 \cdot \sum_{m=0}^{l} \left(\frac{P_l^m}{\sin\theta}\right)^2 m^2 \left(\sigma_{g_l^m}^2 \sin^2 m\phi + \sigma_{h_l^m}^2 \cos^2 m\phi\right),$$

and

$$\sigma_{xy}^2 = \sum_l \left(\frac{a}{r}\right)^{2l+4} (l+1)^2 \cdot \sum_{m=0}^{l} \frac{dP_l^m}{d\theta}\frac{P_l^m}{\sin\theta} m \cos m\phi \sin m\phi \left(\sigma_{g_l^m}^2 - \sigma_{h_l^m}^2\right).$$

Here, correlations between the Gauss coefficients themselves have been ignored. We justify this by noting that the magnitudes of the variances of the Gauss coefficients are similar when derived from sufficient, well-distributed data, implying that estimates of the coefficients are broadly independent (as would be expected near the era of global data coverage from MAGSAT satellite data). The covariance between x and y does not in general vanish. Its mean value over the sphere does, but it is not pointwise zero. However, if the errors on the Gauss coefficients are rotationally invariant (for example, because they are derived from an even data distribution, or resulting from a rotationally invariant error process like the stochastic model of the crustal field (Jackson, 1994)), then they are both a function of l only. In that case, $\sigma_{g_l^m}^2 = \sigma_{h_l^m}^2$, so the covariance σ_{xy}^2 would vanish, and using the spherical harmonic addition theorem and relations derived therefrom (Whaler and Gubbins, 1981, appendix B)

$$\sigma_x^2 = \sigma_y^2 = \frac{1}{2}\sum_l \left(\frac{a}{r}\right)^{2l+4} l(l+1)^3 \sigma_{g_l^m}^2.$$

Thus,

$$\sigma_\alpha^2 = \frac{2\sigma_x^2}{x^2+y^2}.$$

Table 5 shows calculations of σ_x^2, σ_y^2, σ_{xy}^2 and σ_α (expressed in degrees) for the 61 points chosen to represent the null-flux curves in 1980. The covariance term is typically 3 orders of magnitude smaller than the variances, indicating that it can safely be neglected. Note that the angular uncertainty can get very large when the gradient of B_r is small, i.e. when the direction of the normal to the null-flux curve is poorly defined.

References

Amit, H. and P. Olson, Helical core flow from geomagnetic secular variation, *Phys. Earth Planet. Inter.*, **147**, 1–25, 2004.

Backus, G. E., Kinematics of geomagnetic secular variation in a perfectly conducting core, *Philos. Trans. R. Soc. Lond. A*, **263**, 239–266, 1968.

Backus, G. E., Confidence set inference with a prior quadratic bound, *Geophys. J.*, **97**, 119–150, 1989.

Benton, E. R., A simple method for determining the vertical growth-rate of vertical motion at the top of Earth's outer core, *Phys. Earth Planet. Inter.*, **24**, 242–244, 1981.

Bloxham, J., The determination of fluid flow at the core surface from geomagnetic observations, in *Mathematical Geophysics, A Survey of Recent Developments in Seismology and Geodynamics*, edited by N. J. Vlaar, G. Nolet, M. J. R. Wortel, and S. A. P. L. Cloetingh, Reidel, Dordrecht, 1988.

Bloxham, J., Simple models of fluid flow at the core surface derived from geomagnetic field models, *Geophys. J. Int.*, **99**, 173–182, 1989.

Bloxham, J. and D. Gubbins, Geomagnetic field analysis 4: Testing the frozen-flux hypothesis, *Geophys. J. Int.*, **84**, 139–152, 1986.

Bloxham, J. and A. Jackson, Fluid flow near the surface of the Earth's outer core, *Rev. Geophys.*, **29**, 97–120, 1991.

Bloxham, J. and A. Jackson, Time-dependent mapping of the magnetic field at the core-mantle boundary, *J. Geophys. Res.*, **97**, 19,537–19,563, 1992.

Bloxham, J., D. Gubbins, and A. Jackson, Geomagnetic secular variation, *Philos. Trans. R. Soc. Lond. A*, **329**, 415–502, 1989.

Eymin, C. and G. Hulot, On core surface flows inferred from magnetic satellite data, *Phys. Earth Planet. Inter.*, **152**, 200–220, 2005.

Gire, C. and J.-L. Le Mouël, Tangentially geostrophic flow at the core-mantle boundary compatible with the observed geomagnetic secular variation: The large-scale component of the flow, *Phys. Earth Planet. Inter.*, **59**, 259–287, 1990.

Gubbins, D., Finding core motions from magnetic observations, *Philos. Trans. R. Soc. Lond. A*, **306**, 247–254, 1982.

Gubbins, D., Geomagnetic constraints on stratification at the top of Earth's core, *Earth Planets Space*, **59**, 661–664, 2007.

Holme, R., Electromagnetic core-mantle coupling I: Explaining decadal variations in the Earth's length of day, *Geophys. J. Int.*, **132**, 167–180, 1998.

Holme, R., Large-scale flow in the core, in *Core Dynamics*, edited by P. Olson, vol. 8 of *Treatise on Geophysics*, chap. 4, pp. 107–130, Elsevier, 2007.

Holme, R. and N. Olsen, Core surface flow modelling from high-resolution secular variation, *Geophys. J. Int.*, **166**, 518–528, 2006.

Holme, R. and K. A. Whaler, Steady core flow in an azimuthally drifting reference frame, *Geophys. J. Int.*, **145**, 560–569, 2001.

Hulot, G., J. L. Le Mouël, and J. A. Wahr, Taking into account truncation problems and geomagnetic model accuracy in assessing computed flows at the core mantle boundary, *Geophys. J. Int.*, **108**, 224–246, 1992.

Jackson, A., Statistical treatment of crustal magnetisation, *Geophys. J. Int.*, **119**, 991–998, 1994.

Jackson, A., An approach to estimation problems containing uncertain parameters, *Phys. Earth Planet. Inter.*, **90**, 145–156, 1995.

Jackson, A., Kelvin's theorem applied to the Earth's core, *Proc. R. Soc. Lond. A*, **452**, 2195–2201, 1996.

Jackson, A., C. G. Constable, M. R. Walker, and R. L. Parker, Models of Earth's main magnetic field incorporating flux and radial vorticity constraints, *Geophys. J. Int.*, **171**, 133–144, 2007.

Le Mouël, J.-L., C. Gire, and T. Madden, Motions at the core surface in the geostrophic approximation, *Phys. Earth Planet. Inter.*, **39**, 270–287, 1985.

Mosegaard, K. and C. Rygaard-Hjalsted, Probabilistic analysis of implicit inverse problems, *Inverse problems*, **15**, 1999.

Roberts, P. H. and S. Scott, On analysis of the secular variation, 1, A hydromagnetic constraint: Theory, *J. Geomag. Geoelectr.*, **17**, 137–151, 1965.

Voorhies, C. V., Steady surficial core motions: an alternate method, *Geophys. Res. Lett.*, **13**, 1537–1540, 1986.

Voorhies, C. V. and G. E. Backus, Steady flows at the top of the core from geomagnetic-field models—the steady motions theorem, *Geophys. Astrophys. Fluid Dyn.*, **32**, 163–173, 1985.

Whaler, K. A., Does the whole of the Earth's core convect?, *Nature*, **287**, 528–530, 1980.

Whaler, K. A., Fluid upwelling at the core-mantle boundary—resolvability from surface geomagnetic data, *Geophys. J. R. Astron. Soc.*, **78**, 453–473, 1984.

Whaler, K. A., Geomagnetic evidence for fluid upwelling at the core-mantle boundary, *Geophys. J. R. Astron. Soc.*, **86**, 563–588, 1986.

Whaler, K. A. and D. Gubbins, Spherical harmonic analysis of the geomagnetic field: an example of a linear inverse problem, *Geophys. J. R. Astron. Soc.*, **65**, 645–693, 1981.

Wicht, J. and D. Jault, Constraining electromagnetic core-mantle coupling, *Phys. Earth Planet. Inter.*, **111**, 161–177, 1999.

K. A. Whaler (e-mail: kathy.whaler@ed.ac.uk) and R. Holme (e-mail: R.T.Holme@liverpool.ac.uk)